Original Article

A study on observed ultrasonic motor-induced magnetic resonance imaging (MRI) artifacts

Peyman Shokrollahi [a,b,*], *James M. Drake* [a,b], *Andrew A. Goldenberg* [c,d]

[a] *Institute of Biomaterials and Biomedical Engineering, University of Toronto, Toronto, Canada*
[b] *Division of Neurosurgery, The Hospital for Sick Children, Toronto, Canada*
[c] *Institute of Biomaterials and Biomedical Engineering, Engineering Service Inc. University of Toronto, Toronto, Canada*
[d] *Department of Mechanical and Industrial Engineering, University of Toronto, Toronto, Canada*

ARTICLE INFO

ABSTRACT

Background: The safe performance of magnetic resonance imaging (MRI)-guided robot-assisted interventions requires full control and high precision of assistive devices. Because many currently available tools are not MRI-compatible, the characterization of existing tools and development of new ones are necessary. The purpose of this research is to identify and minimize the image artifacts generated by a USM in MR images.

Methods: The behavior of an ultrasonic motor (USM), the most common MRI-safe actuator, in a high-field scanner was investigated. The motor was located in three orientations with respect to the bore axis with the power on or off. The induced image artifacts were compared across four sequences. Three artifact reduction methods (employing ultrashort sequences, slice thickness reductions, and bandwidth increments) were tested.

Results: Signal voids, pileups, and geometric distortions were observed when the motor was off. The artifact size was minimal when the motor shaft was aligned with the bore axis. In addition to the above artifacts, zipper and motion artifacts were noted when the motor was running, and these artifacts increased with increasing motor speed. Increasing the bandwidth slightly reduced the artifacts. However, decreasing the slice thickness from 5 mm to 3 mm and from 5 mm to 1 mm reduced artifact size from 30% to 40% and from 60% to 75%, respectively.

Conclusion: The image artifacts were due to the non-homogenous nature of the static and gradient fields caused by the motor structure. The operating motor interferes with the RF field, causing zipper and motion artifacts.

* *Corresponding author.* Institute of Biomaterials and Biomedical Engineering, University of Toronto, Rosebrugh Building, 164 College Street, Room 407, Toronto, ON M5S3G9, Canada.
E-mail address: peyman.shokrollahi@utoronto.ca (P. Shokrollahi).

At a glance of commentary

Scientific background on the subject

Ultrasonic motors (USMs) are common actuators that can be safely used in developing MRI-compatible robots. When first used in MRI, they generated unsatisfactory results. Lack of compatibility initially shifts researchers' focus from USMs to pneumatic actuators while USMs offer several advantages such as high accuracy, high torque/size ratio, and non-back-drivability.

What this study adds to the field?

This research introduces the types of generated MR image artifacts by an ultrasonic motor used in MRI-compatible surgical robots and provides compensation methods for reducing each type. This study helps engineers for designing MRI-compatible motors and assists clinicians in reducing the generated artifacts.

Ultrasonic motors (USMs) are common magnetic resonance imaging (MRI)-compatible actuators. When first used in MRI, USMs generated unsatisfactory Results. Lack of MRI compatibility initially led researchers to shift their focus from USMs to pneumatic actuators in the development of surgical robots to mitigate compatibility issues such as image distortion, induced image noise, and generated heating. Even though pneumatic and hydraulic systems address some of these compatibility issues, they cannot provide the numerous advantages of USMs, such as high accuracy, high torque/size ratio, and non-back-drivability (i.e., they cannot move when turned off). Moreover, USMs offer the additional advantages of small size, low weight, and compact shape. Thus, USM actuators can be used to perform surgeries safely with high precision and full controllability. The strong capabilities of USMs can be retained and enhancements can be made to address their compatibility issues. This can lead to safer operation of USMs in high field MRI and enable practitioners to accurately and safely operate surgical tools.

Enhancing the compatibility of actuators in the design of surgical robots is required to perform safe surgical interventions in an MRI environment. To eventually turn MRI into a diagnostic tool by developing assistive surgical robots, the interactions between MRI-safe actuators and scanners should be fully elucidated.

Developing MRI-compatible actuators and sensors presents a significant challenge because these devices inherently interfere with the scanner [1]. Three common types of MRI-compatible actuators exist: hydraulic, pneumatic, and ultrasonic actuators. Other types, such as AC or DC actuators, which are commonly used in robotics, have been tested and rejected for MRI because of their high interaction with the magnet due to the ferromagnetic materials that they contain [2].

The hydraulic actuator was the first type of actuator tested to actuate MRI-compatible mechanisms (by Ganesh, in 2004) [3]. Hydraulic actuators are decoupled from electromagnetism by utilizing MRI-compatible materials. Therefore, they do not adversely affect the MR images, nor are they affected by them. However, they are not accepted as appropriate mechanisms because of the risks of leakage, the lack of controllability and reliability, and the requirement for transmission pipes [3]. Pneumatic actuators are another type of common MRI-compatible actuator, considered 'flawless' because they can be decoupled from electromagnetism by utilizing MRI-compatible materials [4]. Pneumatic cylinders function inside the imager with no loss of SNR at no motion and with moderate loss while in motion inside the imager [5]. However, these mechanisms have issues with their controlling systems, resulting in low precision and controllability in motion [4]. The theoretical approach to designing their control algorithms fails because of the complexity and inconsistency of the pneumatic actuators [6]. In addition, some developed pneumatic systems generate low axial force, a maximum of only 46.8 N. This is not sufficient for bone drilling, which requires forces of approximately 100 N [6].

Ultrasonic motors (USMs) are another common type of MRI-safe actuator with numerous advantages. USMs are nonmagnetic devices that generate precisely controllable displacements [7]. Their compactness facilitates the development of small devices operating inside the gantry [8]. This compactness also affords a large workspace for the end-effector, which enables the patient to be placed in any position (supine, lateral, or prone) inside the bore. The compactness of the mechanisms based on USMs also increases the levels of accessibility to the patient. In contrast, neither hydraulic nor pneumatic systems offer these advantages; in most pneumatic systems—such as the MrBot robot, for example—the patient cannot be placed in the decubitus position [9]. In addition, USMs are the best selection because of their high degree of precision [10], their capability to generate forces in high range ($\geq$ 100 N), and the absence of controllability or leakage problems.

The USMs have been used in surgical robots for MRI-guided interventions [8,11]. However, the USM still has limitations preventing complete MRI-compatibility. These limitations cause unwanted effects, such as image artifacts, temperature changes, and deflection forces. The complexity of ultrahigh magnetic fields ($\geq$ 3T) has changed expectations about actuator behavior by amplifying their adverse effects. To overcome these adverse effects, improvement in the design criteria or the development of specific coils is required to reduce the limitation at its source (i.e., the motor). Additionally, optimization of the scanning parameters and the design of specific sequences is needed to mitigate limitations at the target (i.e., the image). This research aimed to identify the types of artifacts generated by motors and their sources. Additionally, this study provides solutions for artifact reduction by quantifying artifacts according to altered sequence parameters.

The presence of the USM induces various types of artifacts on MR images that cause severe image degradation. By identifying the causes, many artifacts can be corrected, minimized, or avoided either before or after data acquisition. Many of the methods that have been applied to reduce artifacts caused by metal implants can be adopted and developed for

motors. However, these methods require examination in the context of a motor.

Although some of the previous studies on ultrasonic motors include designing of new MRI-compatible USMs, this study considers the impact of general ultrasonic motors on MR images [12]. The main objectives of this research are to study the types of image artifacts generated by the USM, provide comparison between them, introduce their sources, and provide compensation methods. In this study, the USM is considered as a system including the motor structure (electrical and mechanical components) and connecting command and power cables. Thus, the impact of this system on the MR images was considered.

Methods

MR images were acquired using a 3.0 T scanner (Achieva, Philips Medical Systems, Best, the Netherlands). The MR scans were performed in two orientations, transverse and coronal (the plane perpendicular to the foot−head axis and the plane in the anterior-posterior direction, respectively) as the patient was supine on the MR bed. Conventional clinical pulse sequences were employed, including T1-weighted spin echo (T1W), T2-weighted turbo spin echo (T2W), turbo spin echo (TSE), and fast field echo (FFE) sequences. The scan parameters were as follows:

T1W: TE = 10 ms, TR = 0.60 s, FOV = 160 × 160 × 150 mm, in-plane voxel size = 1 mm, slice thickness = 5 mm, and flip angle = 70°.
T2W: TE = 80 ms, TR = 3 s, FOV = 160 × 160 × 150 mm, in-plane voxel size = 1 mm, slice thickness = 5 mm, flip angle = 90°, and turbo factor = 5.
TSE: TE = 72 ms, TR = 4 s, FOV = 160 × 160 × 150 mm, in-plane voxel size = 1 mm, slice thickness = 5 mm, flip angle = 90°, and turbo factor = 16.
FFE: TE = 2.8 ms, TR = 12.1 ms, FOV = 160 × 160 × 150 mm, in-plane voxel size = 1 mm, slice thickness = 5 mm, and flip angle = 30°.

The phantoms were leveled inside a 32-channel Philips head coil (Philips Healthcare, Best, the Netherlands) to receive the full signals. The center point of the phantom was aligned with the center point of the coil and positioned in the isocenter using a non-metallic bubble level. The scan procedure and scan parameters were also selected according to the standards [13,14].

The experiment was first performed on the phantom without the presence of a USM (PUMR40, PiezoElectric Technology Co., Ltd., Namyangju, South Korea). The motor includes rotor, stator, bearing, ceramics, base, and case. In addition, the encoder ((MG-30-1000(C), MTL Co., Sagamihara, Japan)) and connecting command and power cables were included. Next, the motor was placed in the immediate vicinity of the phantom and tested in two motor states, on and off. Three orientations were tested. In each case, the motor shaft was oriented toward a particular direction with respect to the bore axis (x, y, and z; Fig. 1). The axis of the phantom was in the direction of the z axis. In the on state, the motor was tested at three speeds
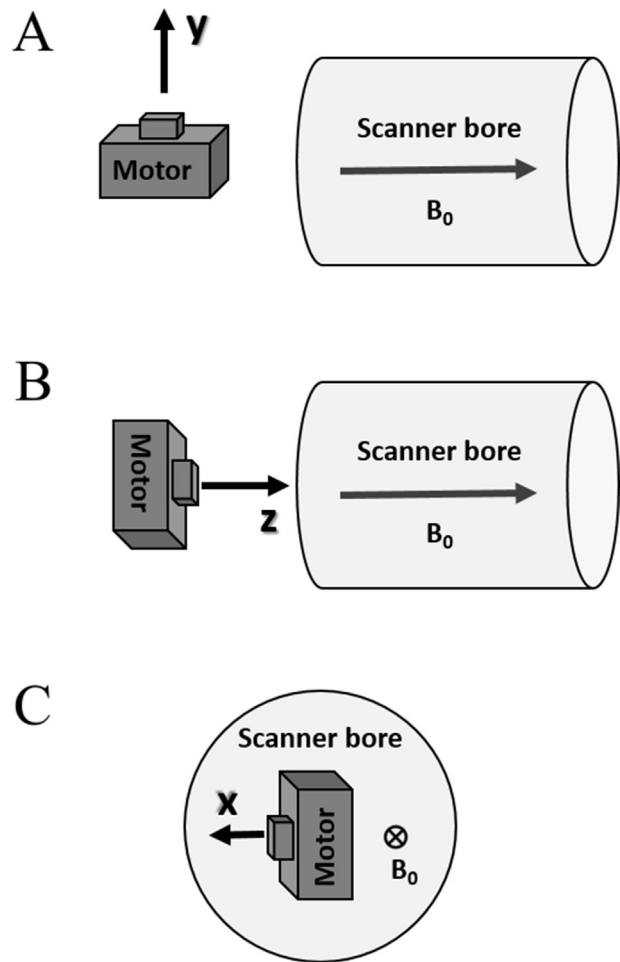

Fig. 1 The orientations of the motor shaft in the scanner bore with respect to B_0, (A) motor shaft in y direction, (B) motor shaft in z direction, and (C) motor shaft in x direction.

(25%, 75%, and 95% of maximum speed) to determine whether the amplitude of the motor's input signal or the motion of the shaft affected the artifacts generated.

Three methods of artifact compensation were tested: sequence selection, slice-thickness (TH) reduction, and bandwidth (BW) increments [15]. These techniques have been recommended for reducing metal artifacts in MR images [16]. To understand the effect of these factors on the artifacts, artifact size was quantified using the four above-mentioned sequences. To compare the effects of the sequences, the same parameters were used to compare sequences. These parameters included slice thickness, BW, NSA (= 1), and TSE factor (= 1). Next, the effects of TH reduction and BW increments were compared. Three slice thicknesses (5 mm, 3 mm, and 1 mm) with two BWs (437 Hz and 875 Hz) were tested using the motor in the y orientation.

The size of the artifacts was measured using a DICOM viewer (RadiAnt DICOM Viewer, version 2.2.9; Meixant, Poznan, Poland) on images collected with the minimum and maximum bandwidth as well as the three slice thicknesses of 5 mm, 3 mm, and 1 mm. The artifacts (including signal voids and pileups) were bounded with oval shapes, and the areas of the ovals were measured in pixels. The measured values were

then divided by the entire area of the phantom (in pixels) to calculate the percentage of area occupied by the artifact in the corresponding slices of the images.

In addition to the above-mentioned sequences, ultrashort echo time (TE) methods (SSH-TSE and STIR-TSE) [17] were employed to reduce artifact size. The sequence specifications were as follows:

SSH-TSE: TE = 90 ms, TR = 15 s, FOV = 150 × 150 × 150 mm, slice thickness = 5 mm, and flip angle = 90°.
STIR-TSE: TE = 15 ms, TR = 4085 ms, FOV = 150 × 150 × 150 mm, slice thickness = 5 mm, and turbo factor = 5.

Results

The induced artifacts included signal voids, pileups, geometric distortions, and zippers. Signal voids, pileups, and geometric distortions were induced when the motor was off (Fig. 2a). Voids are the black regions and pileups are the bright regions in the image. In the absence of voids and pileups, the brightness of the image is uniform. Geometric distortions are the curved lines indicated by the dashed arrows. In fact, they are distorted straight lines of the phantom's gridded image. Zippers and motion artifacts were induced in addition to the above artifacts when the motor was on (Fig. 2b). Zippers are the image noises present in the frequency encoding direction. Motion artifacts are the repetitive shapes (rings indicated in Fig. 2b) in the image along the frequency encoding direction.

When the motor was off, large signal voids were observed in the immediate images of the phantom close to the motor. The sizes of the signal voids and pileups became smaller in image slices that were farther from the motor, and the level of geometric distortion decreased. After the pileups faded, only the geometric distortion remained. Fig. 3 illustrates the reduction in the size and level of the artifacts in the images collected farther from the motor. The artifacts generated with the four mentioned sequences were compared. In all of the sequences, the size of the
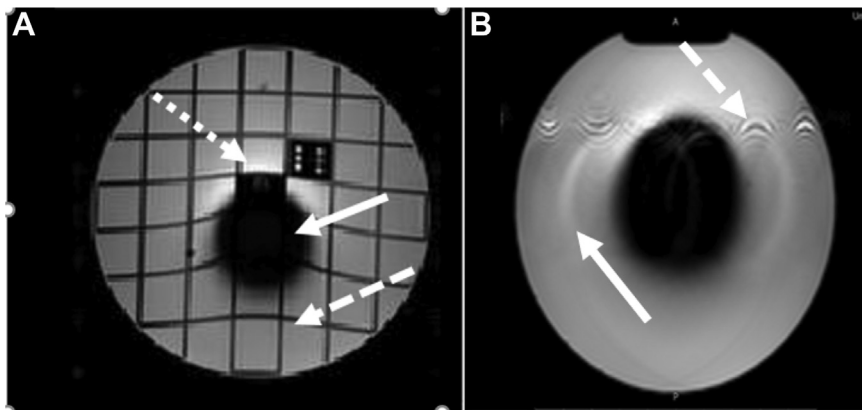

Fig. 2 (A) Example of the artifacts caused by the ultrasonic motor. The solid arrow indicates a signal void, the dotted arrow indicates a signal pileup, and the dashed arrow indicates a geometric distortion. (B) When the motor was on, RF interference caused zipper (dashed arrow) and motion (solid arrow) artifacts.
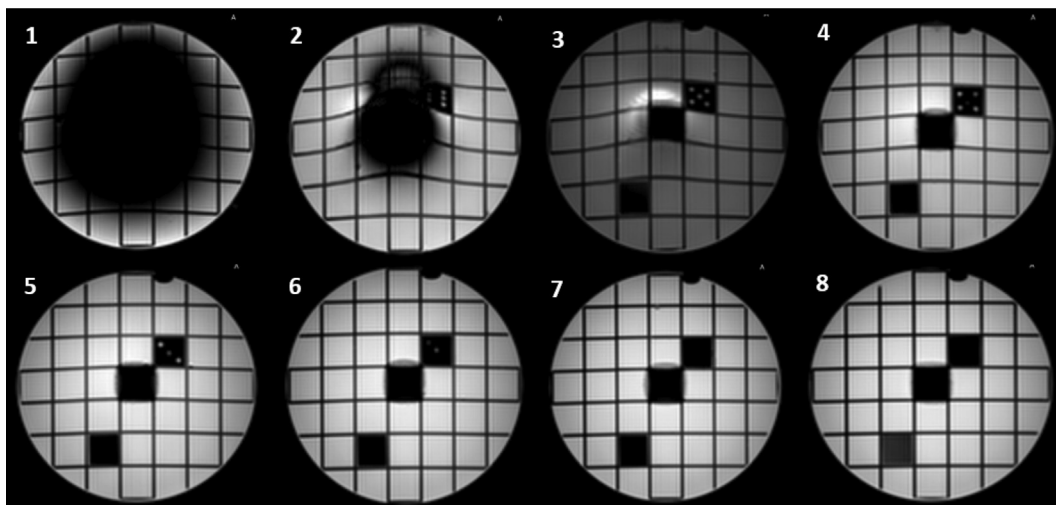

Fig. 3 Eight consecutive slices of the phantom in the presence of the motor scanned with a T2W sequence to indicate the types of generated image artifacts.

signal voids, pileups, and geometric distortions were smallest when the motor was in the z orientation. We further analyzed the effects of motor orientations in Refs. [18,19].

When the motor was on, zippers and motion artifacts were present in the phase-encoding direction with all of the four above-mentioned sequences (Fig. 2). Three motor speeds were tested. Increases in motor speed increased the size and number of zipper and motion artifacts.

The ratio of the artifact area (pixels) to the phantom image area (pixels) was evaluated for the four above-mentioned sequences in the range of 10%—50%. These Results demonstrated that all four sequences generated similarly sized artifacts when the sequence parameters were the same, except FFE had more artifacts. However, the TSE sequence generated fewer artifacts when the TSE factor was increased. Additionally, the SNR was lower in the FFE sequence compared with the other sequences. Therefore, the TSE sequence was considered the base to compare with the ultrashort sequences performed in the next experiments.

The ultrashort TE (SSH-TSE) and STIR sequences reduced artifact size (Fig. 4). Fig. 4 illustrates artifact size at the same distance from the motor in three sequences. The same TH (5 mm) and FOV (150 × 150 × 150 pixels) were used for all of the sequences.

Slice-thickness reduction

Reducing the slice thickness decreased the artifacts. Fig. 5 illustrates signal void reduction in the TSE scans when the slice thickness was reduced. The image slices were taken at the same distance from the motor in all of the images. Signal voids were minimized using the TSE scan at a slice thickness of 0.5 mm, but this change increased scanning time and reduced SNR.

Bandwidth increment

The artifact size did not significantly change with increases in BW. However, the geometric distortion decreased when BW increased. Fig. 6 illustrates the reduction in geometric distortions in the FFE signals when the BW was increased from 237 Hz to 1475 Hz. Increases in BW also improved coronal images. The geometric distortion was corrected at the bottom of the TSE scan images as the BW was increased from 198 Hz to 705 Hz. Further study of the geometric distortion can be found in Ref. [19].

Tables 1—4 present the range of the ratios (percentages) of the artifact area (pixels) to the phantom image area (pixels). The percentages compared in these tables are provided with the minimum and maximum distances from the motor at which the artifact size reached the maximum and minimum, respectively. The distance was calculated by using the number of image slices perpendicular to the axis of the cylindrical phantom. The motor was adjacent to the phantom and it was located on the axis of phantom. The minimum distance is the distance of the motor to the slice with largest artifact. The maximum distance is the distance of the motor to the slice with the smallest artifact.

The maximum artifact size is illustrated for minimum and maximum BW when the slice thickness decreases from 5 to 1 in Fig. 7a and b shows the maximum depth of generated artifacts from the motor's center of mass for three mentioned slice thicknesses and image sequences. This figure shows that decreasing TH and increasing BW result in decreasing the artifact size for all sequences. Generally, T2W has a slightly lower artifact than the others.
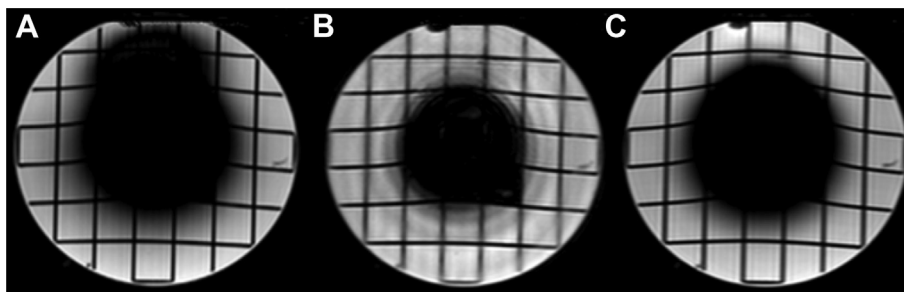

Fig. 4 (A) TSE, (B) SSH-TSE, and (C) STIR-TSE. The ultrashort TE methods reduced motor-induced artifacts.
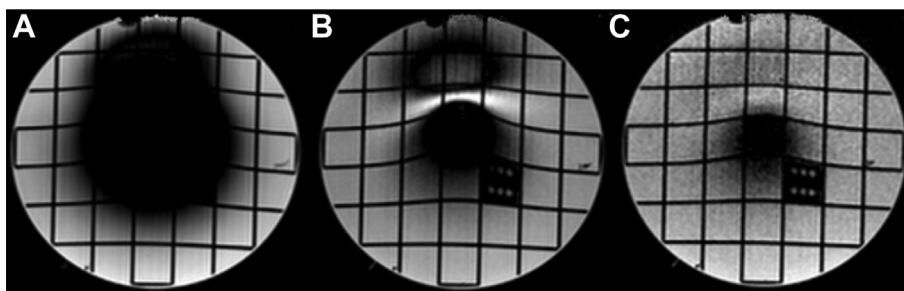

Fig. 5 The slice thickness reductions reduced the signal voids in the TSE scans. Slice thickness of (A) 5 mm, (B) 1 mm, and (C) 0.5 mm.
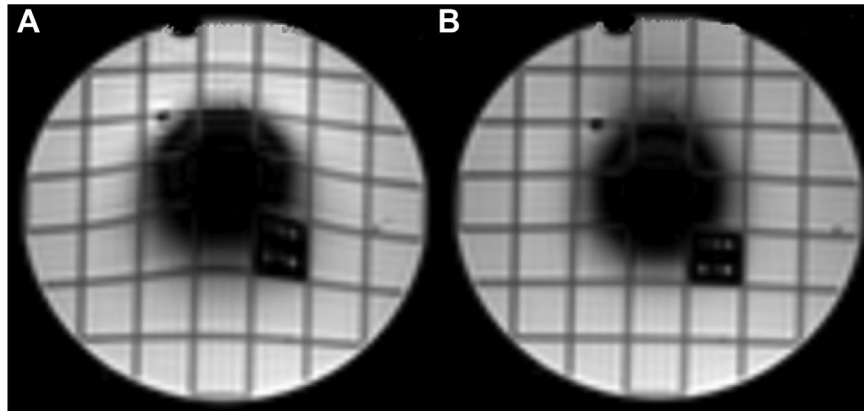
Fig. 6 Geometric distortions were corrected with the FFE sequence as the bandwidth increased from (A) 237 Hz to (B) 1475 Hz.

Table 1 Range of artifact sizes with the T1W sequence to indicate the effects of bandwidth and slice thickness on T1W images.

TH (mm)	BW		Distance from Motor (mm)	
	Minimum	Maximum	Minimum	Maximum
5	12.5%—46.4%	7.4%—46.3%	25	45
3	2.3%—26.8%	2.1%—26.4%	26	38
1	4.9%—18.4%	3.4%—17.0%	26	29

Table 2 Range of artifact sizes with the T2W sequence to indicate the effects of bandwidth and slice thickness on T2W images.

TH (mm)	BW		Distance from Motor (mm)	
	Minimum	Maximum	Minimum	Maximum
5	4.9%—47%	4.5%—46.5%	25	50
3	5.5%—31.9%	4.8%—31.6%	26	40
1	3.2%—18.7%	2.2%—18.4%	26	35

Table 3 Range of artifact sizes with the TSE sequence to indicate the effects of bandwidth and slice thickness on TSE images.

TH (mm)	BW		Distance from Motor (mm)	
	Minimum	Maximum	Minimum	Maximum
5	16.2%—49.2%	10%—47.4%	25	40
3	6%—31.9%	6.7%—31.4%	26	35
1	13.4%—26.2%	2.2%—11.1%	26	32

Table 4 Range of artifact sizes with the FFE sequence to indicate the effects of bandwidth and slice thickness on FFE images.

TH (mm)	BW		Distance from Motor (mm)	
	Minimum	Maximum	Minimum	Maximum
5	18%—51%	18.1%—46%	25	46
3	9%—41.7%	13.5%—39.3%	27	40
1	16%—29%	3.1%—11.3%	25	30

Discussion

The signal voids and pileup artifacts generated when the motor is off were due to the inhomogeneity of the static field caused by the presence of the motor [20]. The motor is made of metallic parts that include the brass part of the motor shaft, the aluminum parts of the motor's body, the electronics of encoder, and the shielded cables attached to the motor. These components affected the gradient field in the slice-selection and frequency encoding directions and generated the above-mentioned artifacts. Zippers were generated from the RF field interference caused by the power and transmission of the encoder signal between the motor and the driver. The motor's power supply and controller were located in the adjacent control room. Both motor cables (i.e., the power and communication cables) were separately shielded inside the scanner room. Both cables were passed through a two-filter D-sub adapter (56F705-003) and grounded through the wall of the scanner room [21]. Although they were shielded, the emission from the cables connecting the motor to the driver still require modification to remove this artifact, because it cannot be corrected after image reconstruction [22]. However, other image artifacts can be reduced by selecting the proper scanning parameters, including the sequence, TH, and BW.

Proper pulse sequence selection reduces artifacts. Employing spin echo techniques (e.g., TSE) reduced the size of the artifact because a 180° refocusing pulse reverses the static field dephasing and refocuses the signal [16]. Because signal dephasing generates signal voids in the image, the image quality is enhanced by reducing the motor artifact. The ultrashort methods and their short TEs meant there was less time for incoherent dephasing of the magnetization [16]. Therefore, fewer artifacts were generated in the images. The two ultrashort echo time sequences, i.e., the ultra-fast spin echo (SSH-TSE) and STIR turbo SE (STIR-TSE) sequences, generated smaller signal voids compared with the TSE sequence when applied to the phantom. The RF signals generated by the water protons are sampled in these sequences faster than they are with the TSE sequences. The
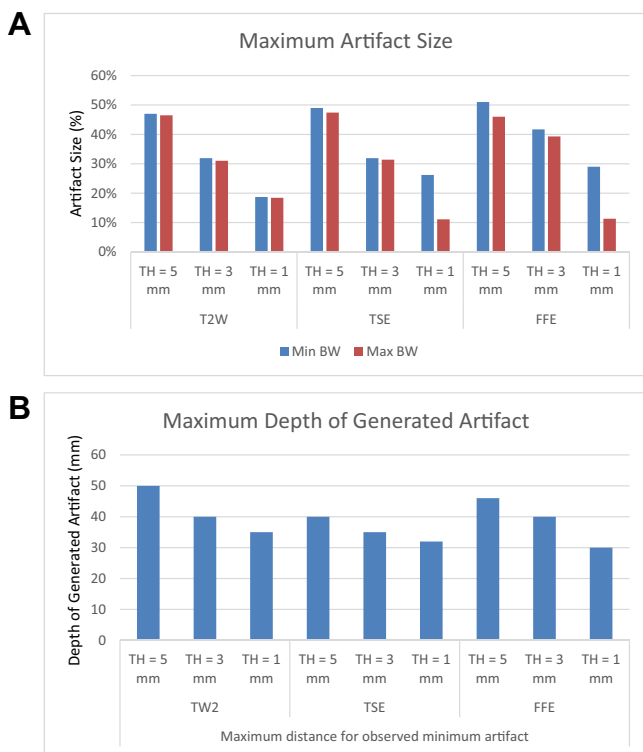
A

B

Fig. 7 (A) The maximum artifact size for three slice thicknesses and three image sequences; (B) The maximum depth of generated artifacts (mm).

presence of the metal components of the motor results in the dephasing of protons and causes image artifacts. The applications of these two ultrashort echo time methods in this experiment illustrated that the time for protons to become dephased was reduced. Subsequently, the generated artifacts were smaller.

A comparison of various slice thicknesses revealed that the reduction of slice thickness significantly reduced the size of the artifact. A reduction in slice thickness from 5 mm to 3 mm reduced the artifact size by 43%, 32%, 34%, and 15%, and a reduction from 5 mm to 1 mm reduced the artifacts by 63%, 60%, 77%, and 75% in the T1W, T2W, TSE, and FFE sequences, respectively. At the expense of longer scan times and SNR degradation, all of the types of motor-induced artifacts became smaller when the slice thickness was decreased. Additionally, the resolution of the image decreased due to the smaller magnetization produced in thinner slices. Therefore, the motor artifacts were minimized in the TSE sequence when the slice thickness was small (0.5 mm).

Increasing the RF receiver bandwidth decreased the geometric distortions induced by the motor but did not significantly reduce the size of the artifacts. The RF signal received by the receiver is mapped according to its frequency-position linear function [23]. However, motor-generated in-homogeneities caused frequency displacements that were unknown to the receiver and resulted in geometric distortions in the images [24]. The use of a steeper gradient field (i.e., a higher BW) reduced this issue.

When the shaft is parallel to the axis of the static magnetic field, the perturbation of the field is less and the size of the susceptibility artifact is reduced. This fact shows the importance of the angle between the motor shaft and the direction of the static magnetic field and is consistent with the results achieved for metal implants [25,26].

In clinical scenarios, voids are the most detrimental artifacts compared to others (zipper, motion, and distortion) because they hinder the observation of anatomical contents. As the USM approaches the field of view in a clinical MRI-guided robotic surgery, this artifact may blacken the region of interest. Zipper and motion artifacts are not clinically harmful because they are clearly distinguishable by their repetitional pattern in the phase-encoding direction. Geometric distortions may have some adverse effect during needle or drill positioning in MR-guided robotic surgery because they could result in inaccurate localization of a target.

This study shows that the voids can be minimized by decreasing the TH and using T2W sequence when the USM is present. Geometric distortion can be minimized by increasing the BW. Reducing the TH results in increasing the imaging time. Thus, the optimum selection of TH can be less than 3 mm, depending on the desirable scanning time.

Conclusions

In conclusion, the artifacts generated by the motor can be decreased by increasing the BW, reducing the TH, and employing ultrashort TE sequences. Additionally, it should be noted that the reduction in image artifacts comes at the cost of an increase in computational time and a reduction in the SNR. A high TSE factor and NSA can be applied to enhance the SNR and the resolution of the images when the motor is present. However, these factors also increase the scanning time. The discussed solutions can be used to assist clinicians to select the most appropriate variables (e.g., TH, BW, or sequence) and values to minimize each particular artifact (zipper, motion, and distortion).

Conflicts of interest

The authors declare that they have no competing interests.

Acknowledgments

REFERENCES

[1] Wang Y, Cole GA, Su H, Pilitsis JG, Fischer GS. MRI compatibility evaluation of a piezoelectric actuator system for a neural interventional robot. Annu Int Conf IEEE Eng Medicine Biol Soc 2009:6072—5.

[2] Moser R, Gassert R, Burdet E, Sache L, Woodtli HR, Erni J, et al. An MR compatible robot technology. Proc Robot Autom IEEE Int Conf 2003;1:670—5.

[3] Ganesh G, Gassert R, Burdet E, Bleuler H. Dynamics and control of an MRI compatible master-slave system with hydrostatic transmission. Proc IEEE Robot Autom Conf 2004;2:1288—94.

[4] Stoianovici D, Song D, Petrisor D, Ursu D, Mazilu D, Mutener M, et al. "MRI Stealth" robot for prostate interventions. Minim Invasive Ther Allied Technol 2007;16:241—8.

[5] Fischer GS, Krieger A, Iordachita I, Csoma C, Whitcomb LL, Fichtinger G. MRI compatibility of robot actuation techniques—a comparative study. In: Int. Conf. Med Image Comput Assist Interv. Berlin: Springer; 2008. p. 509—17.

[6] Song SE, Cho NB, Fischer G, Hata N, Tempany C, Fichtinger G, et al. Development of a pneumatic robot for MRI-guided transperineal prostate biopsy and brachytherapy: new approaches. IEEE Int Conf Robot Autom 2010:258—65.

[7] Gizewski ER, Koeze O, Uffmann K, de Greiff A, Ladd ME, Forsting M. Cerebral activation using a MR-compatible piezoelectric actuator with adjustable vibration frequencies and in vivo wave propagation control. Neuroimage 2005;24:723—30.

[8] Koseki Y, Washio T, Chinzei K, Iseki H. Endoscope manipulator for trans-nasal neurosurgery, optimized for and compatible to vertical field open MRI. In: Dohi T, Kikinis R, editors. Medical image computing and computer-assisted intervention—MICCAI 2002. Berlin: Springer; 2002. p. 114—21.

[9] Mozer PC, Partin AW, Stoianovici D. Robotic image-guided needle interventions of the prostate. Rev Urol 2009;17:7—15.

[10] Cole GA, Harrington K, Su H, Camilo A, Pilitsis JG, Fischer GS. Closed-loop actuated surgical system utilizing real-time in-situ MRI guidance. In: Experimental robotics. Berlin: Springer; 2014. p. 785—98.

[11] Goldenberg AA, Trachtenberg J, Kucharczyk W, Yi Y, Haider M, Ma L, et al. Robotic system for closed-bore MRI-guided prostatic interventions. IEEE ASME Trans Mechatron 2008;13:374—9.

[12] Turowski SG, Seshadri M, Loecher M, Podniesinski E, Spernyak JA, Mazurchuk RV. Performance of a novel piezoelectric motor at 4.7 T: applications and initial tests. J Magn Reson Imag 2008;26:426—32.

[13] American College of Radiology. Site scanning instructions for use of the MR phantom for the ACR MRI accreditation program. Reston, VA: American College of Radiology; 2000.

[14] American College of Radiology. Phantom test guidance for the ACR MRI accreditation program. Reston, VA: American College of Radiology; 1998.

[15] Dietrich O, Reiser MF, Schoenberg SO. Artifacts in 3-T MRI: physical background and reduction strategies. Eur J Radiol 2008;65:29—35.

[16] Hargreaves BA, Worters PW, Pauly KB, Pauly JM, Koch KM, Gold GE. Metal-induced artifacts in MRI. AJR Am J Roentgenol 2011;197:547—55.

[17] Robson MD, Gatehouse PD, Bydder M, Bydder GM. Magnetic resonance: an introduction to ultrashort TE (UTE) imaging. J Comput Assist Tomogr 2003;27:825—46.

[18] Shokrollahi P, Drake JM, Goldenberg AA. Signal-to-noise ratio evaluation of magnetic resonance images in the presence of an ultrasonic motor. Biomed Eng Online 2017;16:45.

[19] Shokrollahi P, Drake JM, Goldenberg AA. Ultrasonic motor-induced geometric distortions in magnetic resonance images. Med Biol Eng Comput 2018;56:61—70.

[20] Price RR, Axel L, Morgan T, Newman R, Perman W, Schneiders N, et al. Quality assurance methods and phantoms for magnetic resonance imaging: report of AAPM nuclear magnetic resonance task group No. 1. Med Phys 1990;17:287—95.

[21] Goldenberg AA, Trachtenberg J, Yi Y, Weersink R, Sussman MS, Haider M, et al. Robot-assisted MRI-guided prostatic interventions. Robotica 2010;28:215—34.

[22] Goldenberg AA, Yang Y, Ma L, Trachenberg J, Kucharczyk W, Haider M, et al. MRI compatible robot with calibration phantom and phantom. https://patentimages.storage.googleapis.com/82/88/17/5925e47e3536ca/US8275443.pdf [Accessed 30 April 2019].

[23] Lu W, Pauly KB, Gold GE, Pauly JM, Hargreaves BA. SEMAC: slice encoding for metal artifact correction in MRI. Magn Reson Med 2009;62:66—76.

[24] Graessner J. Bandwidth in MRI. Magnetom Flash 2013;2:3—8.

[25] Lee MJ, Kim S, Lee SA, Song HT, Huh YM, Kim DH, et al. Overcoming artifacts from metallic orthopedic implants at high-field-strength MR imaging and multi-detector CT. Radiographics 2007;27:791—803.

[26] Suh JS, Jeong EK, Shin KH, Cho JH, Na JB, Kim DH, et al. Minimizing artifacts caused by metallic implants at MR imaging: experimental and clinical studies. AJR Am J Roentgenol 1998;171:1207—13.